Data Integral Invariant Based Beam-hardening Correction: A Simulation Study

Shaojie Tang [a,d†], Kuidong Huang [b], Yunyong Cheng [b], Xuanqin Mou [c], Xiangyang Tang [d‡]

[a]School of Automation, Xi'an University of Posts and Telecommunications, Xi'an, Shaanxi 710121, China
[b]Key Lab of Contemporary Design and Integrated Manufacturing Technology (Northwestern Polytechnical University), Ministry of Education, Xi'an, Shaanxi 710072, China
[c]Institute of Image Processing and Pattern Recognition, Xi'an Jiaotong Univ., Xi'an, Shaanxi 710049, China
[d]Department of Radiology and Imaging Sciences, Emory University School of Medicine, Atlanta, GA 30322, USA

(e-mail: †s.j.tang@hotmail.com, ‡xiangyang.tang@emory.edu)

***Abstract*—In computed tomography (CT), the polychromatic characteristics of x-ray photons emitting from source and absorbed by detector lead to beam-hardening effects in signal detection and image formation, especially in situations where a highly attenuating object (e.g., bone or metal in-plant) is in x-ray beam. Usually, the method called bone bam-hardening correction is employed to suppress the beam-hardening effects, in which either a scaling factor or a vector needs to be pre-determined via tedious physical experiments. Based on the Helgasson-Ludwig consistency condition (HLCC), a data consistency condition based beam-hardening correction has been proposed to avoid such a tedious parameter determination. However, the HLCC requires the involvement of neighboring projection views acquired at a relatively uniform and sufficient sampling rate, which hinders its application in the case wherein the sampling in view is sparse. Having recognized the flexibility of data integral invariant (DII), we extend the HLCC-based method by proposing a DII based objective function in this work. Using computer-simulated projection data, we carry out a simulation study to demonstrate that the process of parameter optimization and performance of the proposed beam-hardening correction method.**

***Index Terms*—CT, Beam-hardening, Consistency Condition, Integral Invariant**

I. Introduction

In x-ray computed tomography (XCT), the polychromatic characteristics of x-ray photons emitting from source and absorbed by detector leads to beam-hardening effects in the formation of projection data[1-7], resulting in severe artifacts (e.g., cupping and/or streak) in reconstructed CT images[1-4].

Beam-hardening artifact and its correction have been investigated since the birth of XCT, which has up to date is still an active research topic. For example, empirical cupping correction (ECC) was proposed for suppressing cupping artifacts[20], in which a polynomial was used to approximate the beam-hardening effects in homogeneous object such as water or soft tissues. Later, an empirical beam-hardening correction (EBHC) method was proposed to deal with the streak artifacts caused by bony structures[21]. Among all existing methods, the water[1-2] and bone corrections[3-4] are still the most frequently used ones in XCT for preclinical and clinical applications. Nevertheless, it is still very hard to effectively carry out a bone-correction over situations where a variety of objects are being imaged[3-4].

In this work, we propose a method based on data consistency condition to determine an optimal scaling factor or vector for bone-correction. Both the HLCC[8-14] and data integral invariant (DII)[15] can be viewed as data consistency condition possessing different characteristics. Lots of researches has been carried out based on the HLCC[8-14, 29], but, as a consistency condition for complete projection data, the HLCC requires the involvement of neighboring projection views acquired at uniform and relatively high sampling rate in view angle, whereas the DII only needs the involvement of a pair of projection views[15, 28]. Hence, a new object function based on the DII is introduced in this work to make bone-correction more applicable and robust over situations in x-ray CT imaging.

II. Theorem Background

A. X-ray Imaging Model

Let $f(x, y) \in C^{\infty}$ be an object function with a compact support in the 2-D real space denoted as ***o*-*xy*** in Fig. 1. In the equi-angular fan-beam geometry, the ideal projection (i.e., monochromatic projection) of $f(x, y)$ is denoted as $g(\beta, \gamma)$ over domain $\{(\beta, \gamma) \mid \beta \in [0, 2\pi), \gamma \in [\gamma_{\min}, \gamma_{\max}]\}$, wherein γ and β are the x-ray's fan-angle and view-angle, respectively.

Let $S(\varepsilon)$ be the source spectrum, which represents the number of photons in range $\varepsilon \in [\varepsilon_{\min}, \varepsilon_{\max}]$, while $Q(\varepsilon)$ be the absorption spectrum of x-ray detector as a photon of energy $\varepsilon \in [\varepsilon_{\min}, \varepsilon_{\max}]$ passes through the detector. $\varepsilon_{\min}$ and $\varepsilon_{\max}$ are the minimal and maximal photon energies, over which the x-ray detector is assumed working at energy integration mode in this work.

The formation of a monochromatic x-ray image at a specific energy $\varepsilon_{mono} \in [\varepsilon_{\min}, \varepsilon_{\max}]$ can be mathematically modeled as

$$g_{mono} = \ln \frac{S(\varepsilon_{mono})Q(\varepsilon_{mono})}{S(\varepsilon_{mono})Q(\varepsilon_{mono})\mathrm{e}^{-\int_L \mu(x,y,\varepsilon_{mono})\rho(x,y)dl}}$$

This work is supported by the New Star Team of XUPT, by the Key Lab of Contemporary Design and Integrated Manufacturing Technology, Northwestern Polytechnical University, Ministry of Education, China, under Grant KF201401, by the Department of Education Shaanxi Province, China, under Grant 15JK1673, and by Shaanxi Provincial Natural Science Foundation of China, under Grant 2016JM8034. X. Tang's work is also supported by the US National Institutes of Health under Grant 2P50AG025688.

$$= \int_L \mu(x,y,\varepsilon_{mono})\,\rho(x,y)\,dl, \tag{1}$$

where μ and ρ represent the mass attenuation coefficient and mass density, and L denotes the integral line corresponding to the x-ray path. For monochromatic imaging, we usually define $f(x, y) = \mu(x, y, \varepsilon_{\text{mono}})\cdot\rho(x, y)$. It is straightforward to understand that the consistency condition holds in projection g_{mono}, as it is the ideal projection of image function $f(x, y)$. In reality, however, an x-ray source emits polychromatic photons and thus the imaging process can only be mathematically modeled as

$$g = \ln \frac{\int_{\varepsilon_{\min}}^{\varepsilon_{\max}} S(\varepsilon)Q(\varepsilon)\,d\varepsilon}{\int_{\varepsilon_{\min}}^{\varepsilon_{\max}} S(\varepsilon)Q(\varepsilon)\,\mathrm{e}^{-\int_L \mu(x,y,\varepsilon)\rho(x,y)dl}\,d\varepsilon}. \tag{2}$$

In polychromatic XCT imaging, we can still define $f(x, y) = \mu(x, y, \varepsilon_{\text{mono}})\cdot\rho(x, y)$, but the consistency condition does not hold in g any more.

B. Water-/Bone-corrections

If a CT image is reconstructed from the polychromatic projection data g, artifacts arise and may degrade diagnostic accuracy and confidence. Thus, it is important to correct beam-hardening effects before image reconstruction.

If the object to be imaged is water-like in its x-ray attenuation characteristic, cupping artifact appears in reconstructed image. The water beam-hardening correction via a polynomial mapping is generally used to suppress the cupping artifact[5-6], in which there are two separate phases[5-6]. In the first phase, water-effective material slabs at different thicknesses are used to acquire polychromatic projections, and a correction polynomial is determined through least square,

$$g_{mono} \approx P_w(g) = \sum_{n=0}^{N} a_n g^n. \tag{3}$$

In the second phase, using the polynomial coefficients $\{a_n\}$, the polychromatic projection g acquired in the scan is mapped into $P_w(g)$ to approximate a monochromatic projection g_{mono}. Note that the performance of water beam-hardening correction depends on the extent to which the object is water-like. Since no spectral information is explicitly required, such a water beam-hardening correction is intrinsically a calibration process.

If both bone and soft tissues exist, streaks artifact may appear due to difference in their attenuation characteristics. In this situation, bone beam-hardening correction is usually used to suppress the cupping and streak artifacts simultaneously[3-4], in which the polychromatic projection g is converted into $P_w(g)$ via water beam-hardening correction. After reconstructed from the corrected projection $P_w(g)$, image f_w is segmented into an image consisting of soft tissues only

$$f_s(x,y) = \begin{cases} f_w(x,y), & f_w(x,y) < T, \\ 0, & f_w(x,y) \geq T, \end{cases} \tag{4}$$

and an image consisting of bone only

$$f_b(x,y) = \begin{cases} 0, & f_w(x,y) < T, \\ f_w(x,y), & f_w(x,y) \geq T, \end{cases} \tag{5}$$

by an empirically determined threshold T. Then, by re-projecting the images f_s, f_b and f_w, one gets

$$g_s = \iint_{(x,y)\in L} f_s(x,y)\,dxdy, \tag{6}$$

$$g_b = \iint_{(x,y)\in L} f_b(x,y)\,dxdy, \tag{7}$$

$$g_w = \iint_{(x,y)\in L} f_w(x,y)\,dxdy. \tag{8}$$

Finally, the polychromatic projection g is corrected to approximate the ideal projection g_{mono} as,

$$g_{mono} \approx P_w(g) + g_w - P_w\left(\ln \frac{\int_{\varepsilon_{\min}}^{\varepsilon_{\max}} S(\varepsilon)Q(\varepsilon)\,d\varepsilon}{\int_{\varepsilon_{\min}}^{\varepsilon_{\max}} S(\varepsilon)Q(\varepsilon)e^{-\mu_s(\varepsilon)g_s-\mu_b(\varepsilon)g_b/\lambda_0}\,d\varepsilon}\right). \tag{9}$$

In *eq.* (9), λ_0 is a scaling factor to adjust the ratio of the reconstructed value in bone image to the mass density of bone and is empirically determined by experiments[3-4]. μ_s and μ_b represent the mass attenuation coefficients of ideal soft and bone tissues, respectively. Note that, the explicit spectra information is only required in the third term on the right-hand side of *eq.* (9). Generally, the spectral information is either supplied by a CT manufacturer or estimated by experimental approach based on, e.g., transmission attenuation experiment.

C. Data Integral Invariant

To determine an optimal scaling factor λ_0 for *eq.* (9) or its corresponding vector $\boldsymbol{c}$ described below, we propose a method based on the DII[15, 28] in this section.

Suppose that there are two projection views indexed by subscripts i = 1, 2, in which γ_i and β_i are the fan-angle of an x-ray and view-angle of the projection view where the x-ray located in. $\boldsymbol{\xi}_i(\beta_i)$ and $\boldsymbol{o}_i$ are respectively the i$^{\text{th}}$ x-ray source position and detector center location, while g(β_i, γ_i) is the ideal projection of the object penetrated by the x-ray from the i^{th} source position on the i^{th} detector, and $r_i = \left\|\boldsymbol{\xi}_i(\beta_i)-\boldsymbol{o}\right\|$, $D_i = \left\|\boldsymbol{\xi}_i(\beta_i)-\boldsymbol{o}_i\right\|$. As $r = r_i$ and $D = D_i$, i = 1, 2, there exist a data integral invariant (DII) condition[15, 28],

$$\int_{\gamma_{\min}}^{\gamma_{\max}} \frac{g_{mono}(\beta_1,\gamma_1)}{\cos(\Delta\beta/2-\gamma_1)}d\gamma_1 = \int_{\gamma_{\min}}^{\gamma_{\max}} \frac{g_{mono}(\beta_2,\gamma_2)}{\cos(\Delta\beta/2+\gamma_2)}d\gamma_2, \tag{10}$$

where $\Delta\beta = \beta_2-\beta_1$. Note that the HLCC requires a combination of information from neighboring projection views, but the DII relates to a pair of projection views only. This is the underlying reason that we introduce the DII-based method in this paper.

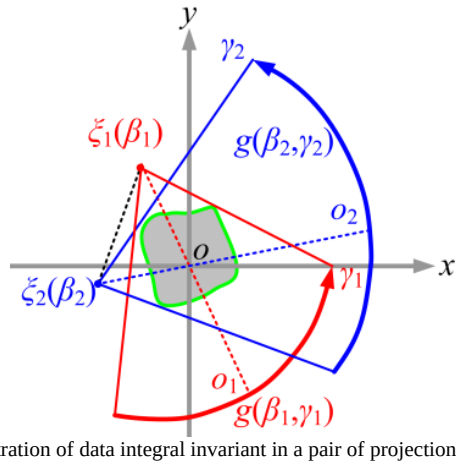

Fig. 1. Illustration of data integral invariant in a pair of projection views.

D. Proposed Method

To demonstrate the principle of proposed method, here we only consider the equi-angular fan-beam geometry and a circular trajectory, in which $r = r_i$, $D = D_i$, and $i = 1, 2$ as in *eq*. (10). In order to correct for beam-hardening effects, by combining the water and bone beam-hardening corrections and DII, we propose the following objective function and its minimization to determine an optimal scaling factor λ_0

$$\Phi_0(\lambda_0) = \int_0^{2\pi}\int_0^{2\pi}\left(\int_{\gamma_{\min}}^{\gamma_{\max}} \frac{g_{mono}(\beta_1,\gamma)}{\cos(\Delta\beta/2-\gamma)} - \frac{g_{mono}(\beta_2,\gamma)}{\cos(\Delta\beta/2+\gamma)}d\gamma\right)^2 d\beta_1 d\beta_2, \quad (11)$$

Note that the integrand is actually *eq*. (10).

Unfortunately, in practice it is not easy to exactly determine the spectra $S(\varepsilon)$ and $Q(\varepsilon)$. Then, a polynomial approximation with respect to variables g_s and g_b need to be carried out,

$$P_w\left(\ln\frac{\int_{\varepsilon_{\min}}^{\varepsilon_{\max}} S(\varepsilon)Q(\varepsilon)d\varepsilon}{\int_{\varepsilon_{\min}}^{\varepsilon_{\max}} S(\varepsilon)Q(\varepsilon)e^{-\mu_s(\varepsilon)g_s(\beta_i,\gamma)-\mu_b(\varepsilon)g_b(\beta_i,\gamma)/\lambda_0}d\varepsilon}\right) \approx \boldsymbol{g}_i \bullet \boldsymbol{c}', i = 1,2, \quad (12)$$

where $\boldsymbol{g}_i = [g_s\ g_b\ g_s^2\ g_b^2\ g_s g_b\ g_b^{0.5}]_i$ and depends on the x-ray path (β_i, γ) and $\boldsymbol{c} = [c_1\ c_2\ c_3\ c_4\ c_5\ c_6]$ is the coefficient vector. The objective function $\Phi_0(\lambda_0)$ can be further simplified into

$$\Phi_1(\boldsymbol{c}) = \int_0^{2\pi}\int_0^{2\pi}\left(\int_{\gamma_{\min}}^{\gamma_{\max}} \frac{\boldsymbol{g}_1\bullet\boldsymbol{c}' - P_w(\hat{g}(\beta_1,\gamma))}{\cos(\Delta\beta/2-\gamma)} - \frac{\boldsymbol{g}_2\bullet\boldsymbol{c}' - P_w(\hat{g}(\beta_2,\gamma))}{\cos(\Delta\beta/2+\gamma)}d\gamma\right)^2 d\beta_1 d\beta_2. \quad (13)$$

The scaling factor λ_0 and its corresponding vector $\boldsymbol{c}$ can then be determined by minimizing the objective functions $\Phi_0(\lambda_0)$ and $\Phi_1(\boldsymbol{c})$ via least square (namely $\Phi_0(\lambda_0)$ and $\Phi_1(\boldsymbol{c})$ methods).

E. Numerical Implementation

To numerically implement the minimization of the aforementioned objective functions, we re-express the objective function $\Phi_0(\lambda_0)$ as[29]

$$\Phi_0(\lambda_0) = \sum_{j=1}^{\max j}\left(\phi_j(\lambda_0)\right)^2, \quad (14)$$

where $\phi_j(\lambda_0) = \psi_{\beta_1}^0(\lambda_0) - \psi_{\beta_2}^0(\lambda_0)$, the subscript j is the index of the combination of view angles β_1 and β_2, and max j can be determined by *eq*. (11). Because $\phi_j(\lambda_0)$ is a nonlinear function of the variable λ_0, a nonlinear least-square method is required to minimize $\Phi_0(\lambda_0)$ as follows:

$$\lambda_0^{k+1} = \lambda_0^k - \left(A_k' A_k\right)^{-1} A_k' \phi^k, \quad (15)$$

where

$$A_k = \left[\nabla\phi_1(\lambda_0^k)\ \ \nabla\phi_2(\lambda_0^k)\cdots\nabla\phi_{\max j}(\lambda_0^k)\right]', \quad (16)$$

$$\phi^k = \left[\phi_1(\lambda_0^k)\ \ \phi_2(\lambda_0^k)\cdots\phi_{\max j}(\lambda_0^k)\right]', \quad (17)$$

λ_0^k is the k^{th} step of approximation for the minimum value point of $\Phi_0(\lambda_0)$. The iteration process will be terminated as soon as certain stopping criteria are satisfied. Here, a maximal iteration number max k is used as the stopping criterion. Finally, the determined $\lambda_0^{\max k}$ is substituted into the following bone-correction formula for beam-hardening correction,

$$g = P_w(\hat{g}) + g_w - P_w\left(\ln\frac{\int_{\varepsilon_{\min}}^{\varepsilon_{\max}} S(\varepsilon)Q(\varepsilon)d\varepsilon}{\int_{\varepsilon_{\min}}^{\varepsilon_{\max}} S(\varepsilon)Q(\varepsilon)e^{-\mu_s(\varepsilon)g_s-\mu_b(\varepsilon)g_b/\lambda_0^{\max k}}d\varepsilon}\right). \quad (18)$$

Similarly, the objective function $\Phi_1(\boldsymbol{c})$ is re-expressed as[29]

$$\Phi_1(\boldsymbol{c}) = \sum_{j=1}^{\max j}\left(\phi_j(\boldsymbol{c})\right)^2, \quad (19)$$

where $\phi_j(\boldsymbol{c}) = \psi_{\beta_1}^0(\boldsymbol{c}) - \psi_{\beta_2}^0(\boldsymbol{c})$, and max$j$ can be determined by *eq*. (13). Because $\phi_j(\boldsymbol{c})$ is a linear function of the variable c, a linear least-square method can be adopted to minimize $\Phi_1(\boldsymbol{c})$ as follows:

$$\boldsymbol{c}^1 = \boldsymbol{c}^0 - \left(A_0' A_0\right)^{-1} A_0' \phi^0, \quad (20)$$

where

$$A_0 = \left[\nabla\phi_1(\boldsymbol{c}^0)\ \ \nabla\phi_2(\boldsymbol{c}^0)\cdots\nabla\phi_{\max j}(\boldsymbol{c}^0)\right]', \quad (21)$$

$$\phi^0 = \left[\phi_1(\boldsymbol{c}^0)\ \ \phi_2(\boldsymbol{c}^0)\cdots\phi_{\max j}(\boldsymbol{c}^0)\right]', \quad (22)$$

$$\boldsymbol{c}^0 = \boldsymbol{0}. \quad (23)$$

Finally, the determined $\boldsymbol{c}^1$ is adopted for beam-hardening correction as follows:

$$g = P_w\left(\hat{g}\right) + g_w - \boldsymbol{g}\cdot\left(\boldsymbol{c}^1\right)', \tag{24}$$

where $\boldsymbol{g} = [g_s\ g_b\ g_s^2\ g_b^2\ g_s g_b\ g_b^{0.5}]$.

III. EXPERIMENTAL EVALUATION

The projection data of FORBILD head phantom simulated by computer are used to assess the capability and performance of the proposed methods[7, 17].

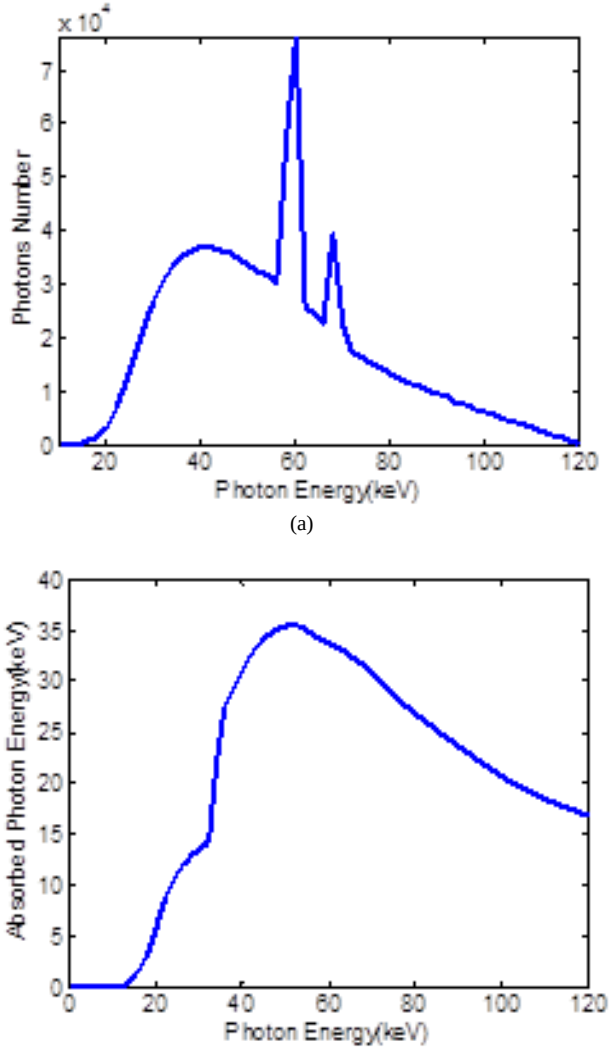

Fig. 2. (a) Emitting spectrums of an x-ray source with 120 *kVp* tube potential and (b) Absorption spectrum of CsI x-ray detector.

The circular scanning trajectory is of radius r = 541*mm*. An equi-angular detector is positioned opposite to the x-ray source about the origin $\boldsymbol{o}$. The arced detector array consists of 888 cells with a fan-angle of 54.89°. 1,160 projections are uniformly acquired in a full scan. Reconstructed images are in 1,024× 1,024 matrices with $0.2344 \times 0.2344 mm^2$ pixel size. The emitting spectrum of x-ray source[18] $S(\varepsilon)$ is shown in Fig. 2(a), while the absorption spectrum of a CsI detector[19] $Q(\varepsilon)$ is shown in Fig. 2(b), wherein the energy sampling interval is 1 *keV*.

We assume that there is no Compton scatter involved in data acquisition, as it is removed or almost removed by the device called anti-scatter grid in clinical CT. The tube potential is 120 *kVp*, while, a monochromatic case of 55 *keV* is simulated to serve as benchmark. Noise is simulated by assuming 3×10^5 photons for each x-ray using the noise model[7],

$$g_n = \ln\frac{\int_{\varepsilon_{\min}}^{\varepsilon_{\max}} \mathbf{P}\left(S(\varepsilon)\right)Q(\varepsilon)\,d\varepsilon}{\int_{\varepsilon_{\min}}^{\varepsilon_{\max}} \mathbf{P}\left(S(\varepsilon)e^{-\int_L \mu(x,y,\varepsilon)\rho(x,y)dl}\right)Q(\varepsilon)\,d\varepsilon}, \tag{25}$$

where **P** represents generation of a random number observing the Poisson distribution. The addition of noise is to evaluate the stability in objective function minimization, rather than the performance of image reconstruction algorithm.

IV. EXPERIMENTAL RESULTS

The FBP algorithm is used in this work for image reconstruction, though iterative algorithm can also be used. Fig. 3 shows the images reconstructed from the monochromatic/ polychromatic projection data with/without noise. From the polychromatic images in Fig. 3(b-b') and the difference images in Fig. 3(c-c'), it is observed that there are cupping and severe streak artifacts. Then, we studied the convergence of $\Phi_0(\lambda_0)$ method. To minimize the objective function $\Phi_0(\lambda_0)$, we set k_{max}=10 based on experiments. According to physical meaning of the scaling factor [3-4], we assume λ_0>1 and thus 1.0 is chosen as a reasonable initial value of λ_0. As shown in Fig. 4, the minimization process converges quickly after about 4 iterations, indicating a very fast and stable convergence.

The performance of beam-hardening correction is assessed by comparing the reconstructed polychromatic images with/without beam-hardening correction. Presented in Fig. 5 are the images reconstructed from the noise-free polychromatic projection data, along with the difference images between the corrected and uncorrected results. The results in Fig. 5 show that both existing water beam-hardening correction method and the proposed algorithm are effective in suppressing cupping artifacts. However, there exist streak artifacts in the image with water beam-hardening correction only (see Fig. 5(a) and (a') and their comparison with Fig. 3(c). As shown in Fig. 5(b-b') and (c-c'), the proposed $\Phi_0(\lambda_0)$ and $\Phi_1(\boldsymbol{c})$ methods outperform the water beam-hardening correction in suppression of streak artifact (comparing Fig. 5(b) and (c) with Fig. 3(c)).

Shown in Fig. 6 are the images reconstructed from noisy polychromatic data, along with the corresponding difference images. The performance of beam-hardening correction in Fig. 6 is similar to that in Fig. 5, demonstrating robustness of the proposed methods over noise.

V. DISCUSSIONS AND CONCLUSIONS

In this work, we proposed a novel bone beam-hardening correction algorithm and carried out a performance evaluation. Different from the HLCC-based method, which requires involvement of neighboring projection views, the proposed method is more applicable in practice because it only requires that a pair of projection views be available. It is worthwhile noting that the proposed method can also be carried out in

cone-beam CT, C-arm CT and helical/spiral CT, as long as *eq*. (10) is adequately extended to the corresponding geometry.

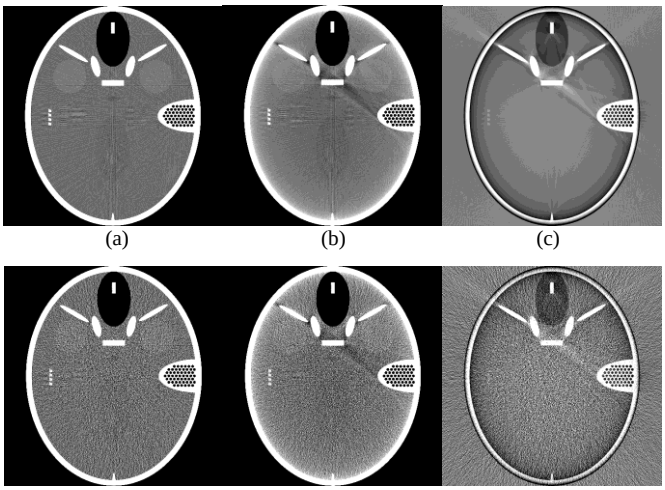

Fig. 3. Images reconstructed from computer-simulated projection data. 1st and 2nd rows are noise-free and noisy images. Left, middle and right columns correspond to monochromatic (55 *keV*), polychromatic (120 *kVp*), and their difference (display window [-100 100] HU).

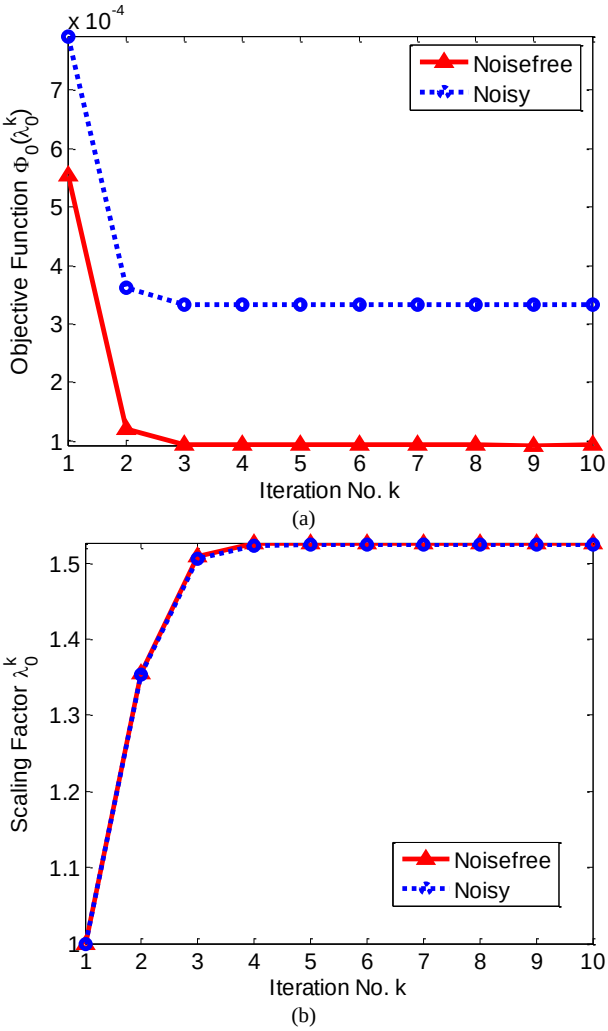

Fig. 4. Convergence curves of (a) objective function $\Phi_0(\lambda_0^k)$ and (b) scaling factor λ_0^k with respect to iteration number *k*.

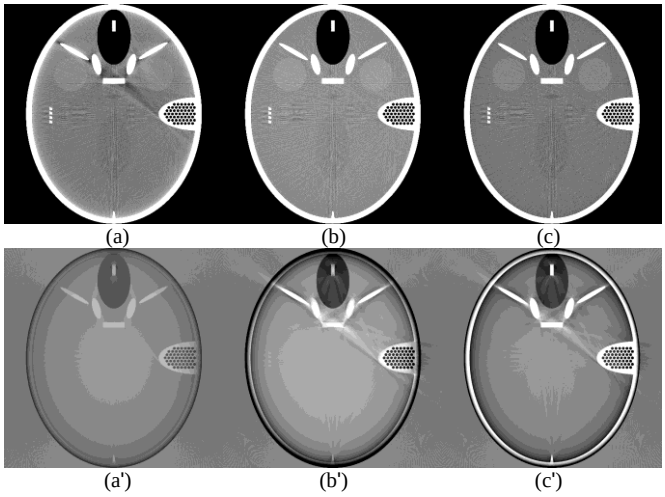

Fig. 5. Images reconstructed from noise-free polychromatic data: (a) With water beam-hardening correction only, (b) and (c) with the $\Phi_1(c)$ and $\Phi_0(\lambda_0)$ methods. (a', b', c') are the difference between Fig. 5(a), (b) and (c) and the uncorrected result (Fig. 3 (b)) (display window [-100 100] HU).

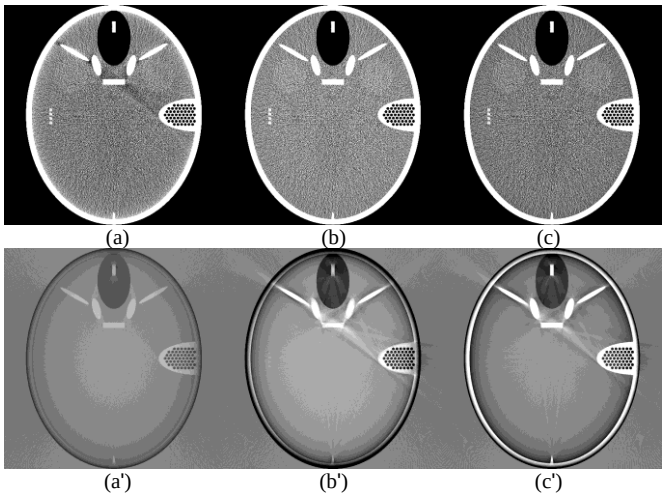

Fig. 6. Images reconstructed from noisy polychromatic data in layout the same as Fig. 5.

REFERENCES

[1] W. D. McDavid, R. G. Waggener, W. H. Payne, and M. J. Dennis, "Correction for spectral artifacts in cross-sectional reconstruction for X-rays," Med. Phys. 4, 54-57 (1977).

[2] G. T. Herman, "Correction for beam hardening in computed tomography," Phys. Med. Biol. 24, 81-106 (1979).

[3] P. Joseph and R. Spital, "A method for correcting bone induced artifacts in computed tomography scanners," J. Comput. Assist. Tomo. 2, 100-108 (1978).

[4] O. Nalcioglu and R. Y. Lou, "Post-reconstruction method for beam hardening in computerised tomography," Phys. Med. Biol. 24, 330-340 (1979).

[5] B. De Man, J. Nuyts, P. Dupont, G. Marchal, and P. Suetens, "Metal streak artifacts in x-ray computed tomography: a simulation study," IEEE Trans. Nucl. Sci. 46, 691-696 (1999).

[6] S. Tang, H. Yu, H. Yan, D. Bharkhada, and X. Mou, "X-ray projection simulation based on physical imaging model," J. X-ray Sci. Tech. 14, 177-189 (2006).

[7] S. Tang, X. Mou, Y. Yang, Q. Xu, and H. Yu, "Application of projection simulation based on physical imaging model to the evaluation of beam hardening corrections in X-ray transmission tomography," J. X-ray Sci. Tech. 16, 95-117 (2008).

[8] F. Natterer, "The Mathematics of Computerized Tomography," John Wiley & Sons Ltd, (1986).

[9] M. Li and D. Wang, "CT image reconstruction from limited information," Proc. SPIE 2390, 116-126 (1995).

[10] S. Basu and Y. Bresler, "Uniqueness of tomography with unknown view angles," IEEE Trans. Image Process. 9, 1094-1106 (2000).

[11] T. J. Wang and T. W. Sze, "The image moment method for the limited range CT image reconstruction and pattern recognition," Pattern Recognition 34, 2145-2154 (2001).

[12] H. Yu, Y. Wei, J. Hsieh, and G. Wang, "Data consistency based translational motion artifact reduction in fan-beam CT," IEEE Trans. Med. Imaging 25, 792-803 (2006).

[13] H. Yu and G. Wang, "Data consistency based rigid motion artifact reduction in fan-beam CT," IEEE Trans. Med. Imaging 26, 249-260 (2007).

[14] J. Xu, K. Taguchi, and B. M. W. Tsui, "Statistical projection completion in x-ray CT using consistency conditions," IEEE Trans. Med. Imaging 29, 1528-1540 (2010).

[15] Y. Wei, H. Yu, and G. Wang, "Integral Invariants for Computed Tomography," IEEE Signal Processing Letters 13, 549-552 (2006).

[16] H. Yu and G. Wang, "Compressed sensing based interior tomography," Phys. Med. Biol. 54, 2791-2805 (2009).

[17] G. Lauritsch and H. Bruder, "head phantom," http://www.imp.uni-erlangen.de/phantoms/head/head.html, (1998).

[18] T. R. Fewell, R. E. Shuping, and K. R. Hawkins, "Handbook of computed tomography x-ray spectra," Washington, D.C.: HHS Publication (FDA) 81-8162, 27-29 (1981).

[19] J. A. Rowlands and K. W. Taylor, "Absorption and noise in cesium iodide x-ray image intensifiers," Med. Phys. 10, 786-795 (1983).

[20] M. Kachelrieß, K. Sourbelle, and W. A. Kalender, "Empirical cupping correction: A first-order raw data precorrection for cone-beam computed tomography," Med. Phys. 33, 1269-1273 (2006).

[21] Y. Kyriakou, E. Meyer, D. Prell, and M. Kachelrieß, "Empirical beam hardening correction (EBHC) for CT," Med. Phys. 37, 5179-5187 (2010).

[22] G. Chen and S. Leng, "A new data consistency condition for fan-beam projection data," Med. Phys. 32, 961-967 (2005).

[23] S. Leng, B. Nett, M. Speidel, and G. Chen, "Motion artifact reduction in fan-beam and cone-beam computed tomography via the Fan-beam Data Consistency Condition (FDCC)," Proc. SPIE 6510, 65101W (2007).

[24] F. John, "The ultrahyperbolic equation with four independent variables," J. Duke Math. 4, 300-322 (1938)

[25] S. K. Patch, "Computation of Unmeasured Third-Generation VCT Views From Measured Views," IEEE Trans. Med. Imaging 21, 801-813 (2002).

[26] S. K. Patch, "Consistency conditions upon 3D CT data and the wave equation," Phys. Med. Biol. 47, 1-14 (2002).

[27] M. Defrise, F. Noo, and H. Kudo, "Improved two-dimensional rebinning of helical cone-beam computerized tomography data using John's equation," Inverse Probl. 19, S41-S54 (2003).

[28] S. Tang, Q. Xu, X. Mou, and X. Tang, "The mathematical equivalence of consistency conditions in the divergent-beam computed tomography," Journal of X-Ray Science and Technology 20, 45-68 (2012).

[29] S. Tang, X. Mou, Q. Xu, Y. Zhang, J. Bennett, and H. Yu, "Data consistency condition–based beam-hardening correction," Optical Engineering 50, 076501 (2011).

Shaojie Tang received the Ph.D. degree from the School of Electronic and Information Engineering, Xi'an Jiaotong University, Xi'an, China, in 2010. He is currently an Associate Professor with the School of Automation, Xi'an University of Posts and Telecommunications, Xi'an, China, and serves as a co-researcher with the Department of Radiology and Imaging Sciences, Emory University School of Medicine, Atlanta, USA. His research interests include medical imaging, image processing, image analysis and computer vision.